

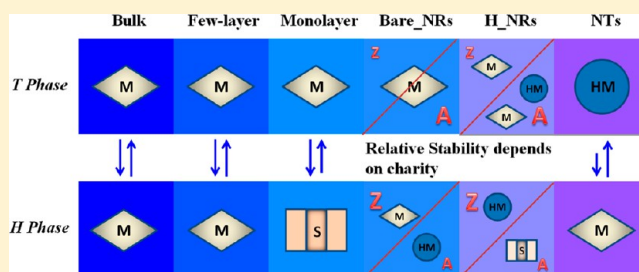
Versatile Electronic Properties of VSe₂ Bulk, Few-Layers, Monolayer, Nanoribbons, and Nanotubes: A Computational Exploration

Fengyu Li, Kaixiong Tu, and Zhongfang Chen*

Departments of Physics and Chemistry, University of Puerto Rico-Rio, Piedras Campus, P.O. Box 23346, San Juan, PR 00931, United States

Supporting Information

ABSTRACT: Density functional theory computations were performed to investigate the stabilities and magnetic and electronic properties of VSe₂ bulk, few-layers, monolayer, and its derived nanoribbons (NRs) and nanotubes in both *T* and *H* phases. All these materials are ferromagnetic, but exhibit versatile electronic properties. The VSe₂ bulk and few-layers in either *T* or *H* phase, and *T* monolayer are metallic, while the *H* monolayer is a semiconductor. For nanoribbons, the zigzag NRs in both *T* and *H* phases and the armchair NRs in *T* phase are metallic, while the armchair NRs in *H* phase are half-metallic. The edge hydrogenation can retain or amend the electronic property of the pristine NRs depending on the chirality and phases. Regardless of the chirality, nanotubes in *T* phase are half-metallic, while those in *H* phase are metals. These findings provide a simple and effective route to tune the electronic properties of VSe₂ nanostructures in a wide range and also facilitate the design of VSe₂-based nanodevices.



1. INTRODUCTION

Following the successful exfoliation of graphene,¹ many two-dimensional (2D) layered noncarbon materials,^{2,3} such as BN and MoS₂, have been experimentally realized and theoretically investigated. These 2D materials are bringing revolutions to numerous advanced applications due to their unique and fascinating physical and chemical properties. Moreover, the properties are tunable in these 2D materials and their related one-dimensional (1D) nanoribbons, for example, by either edge modification or surface functionalizations, and by rolling them into 1D nanotubes with different chirality and diameters.

Among the noncarbon 2D materials, transition-metal dichalcogenides (TMDs) have been extensively studied.^{4–8} The layered TMDs consist of one transition-metal atom between two chalcogen atoms forming covalently bonded sheets with formula MX₂, where M is a transition metal and X are chalcogen atoms. Adjacent sheets are bonded to each other with weak van der Waals forces, leading to highly anisotropic properties. The anisotropy of the materials leads to interesting properties connected to the quasi low dimensionality, and therefore TMDs serve as an important model system for 2D phenomena. Typically, the properties of 2D nanomaterials are dependent on the thickness. Taking molybdenum disulfide, one of the mostly studied TMDs, as an example, the MoS₂ monolayer exhibits a ~1.8 eV direct band gap while a bilayer MoS₂ exhibits an indirect band gap of ~1.5 eV.⁹

Vanadium diselenide (VSe₂) is a typical TMD material.¹⁰ The VSe₂ monolayer is composed of metal V atoms sandwiched between two Se atom (Figure 1a), and the Se–V–Se layers are stacked in the (001) direction without lateral

displacement forming trigonal (*T*) phase polytype crystal (Figure S1a) in the bulk. Though holding very similar sandwich structure with MoS₂ (Figure 1b), VSe₂ exists only in *T* phase (space group: *P*6₃*mc*) in nature, while MoS₂ adopts the hexagonal (*H*) phase (space group: *P*6₃/*mmc*) in bulk with the Mo atoms in octahedral coordination with S atoms.

For VSe₂ bulk crystal, extensive studies have been performed to investigate its charge density wave (CDW) transitions^{11–18} and intercalation properties,^{19–24} due to the interaction between the electron and phonon subsystem,²⁵ and the ability to form intercalation complexes with foreign atoms or molecules incorporated between the layers.

Meanwhile, the VSe₂ thin films have been synthesized by different approaches, such as chemical vapor transport,²⁶ chemical vapor deposition,^{27,28} and electron beam evaporation.²⁹ Quite recently, Xie's group successfully synthesized 2D VSe₂ ultrathin (four to eight layers) nanosheets by liquid exfoliation of a bulk VSe₂ crystal in formamide solvent,³⁰ and they found that such nanostructures retain the electronic and magnetic characters like its 3D bulk phase, and their simulations on *T*-phase bulk and monolayer reproduced well the experimentally observed metallic properties.

On the other hand, the *H*-type single-layer components were found in the *R* polytype VSe₂ bulk. Spiecker et al.²⁶ observed the *T* → *R* polytype transformation in the thin VSe₂ surface layer, which was induced by Cu deposition. Such transformations

Received: July 16, 2014

Revised: August 12, 2014

Published: August 13, 2014

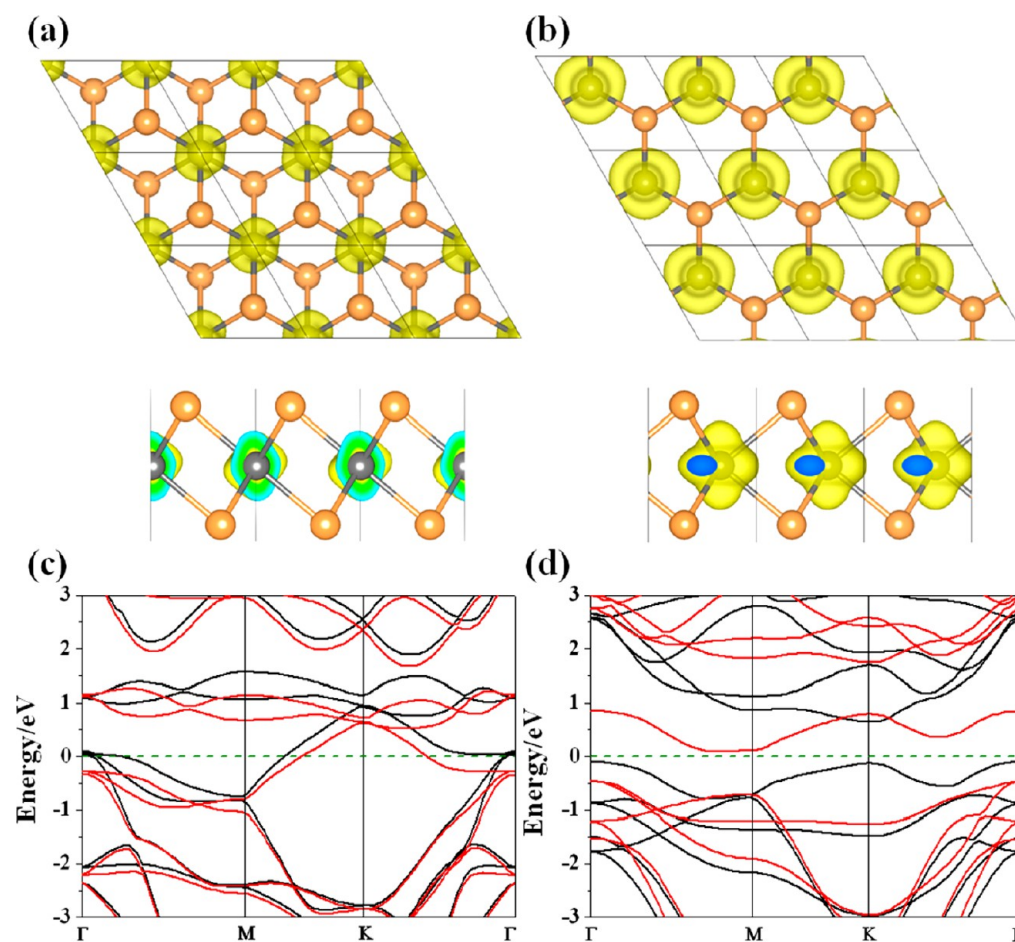


Figure 1. Magnetism distributions (top and side views) of 2D single-layer VSe_2 geometries (3×3 supercell) in the T (a) and H phases (b), as well as their corresponding band structures (c, d). The gray and khaki atoms represent V and Se atoms, respectively. The isosurface value was set to be $0.008 \text{ e}/\text{\AA}^3$. The spin-polarized band structures with both spin-up and spin-down channels are presented in black and red, respectively. The Fermi energy is denoted by a green dashed line.

were also found when electrochemically intercalating Cu into bulk VSe_2 ³¹ or intercalating K into VSe_2 in vacuum.³² In each single-layer component of the R polytype (see Figure S1d), the V atoms are in trigonal prismatic coordination with Se atoms, representing a H -type monolayer (Figure 1b). Note that the only difference between H - MoS_2 (Figure S1b) and R - VSe_2 (Figure S1d) bulk is the stacking patterns of the sandwich layers: the adjacent layers were stacked by tilting the crystal lattice by an angle (θ) of $\sim 17^\circ$ and $\sim 20^\circ$ from the c -axis orientation, respectively.

Exploring the VSe_2 nanostructures is helpful to gain insights into the properties of VSe_2 at the atomic scale. So far, single-layer VSe_2 sheet has not been experimentally realized; a systematic theoretical investigation on its structure and properties can not only enhance our understanding to their intrinsic characteristics but also facilitate their applications. Despite some theoretical studies on the electronic structures of VSe_2 bulk^{33,34} and T -type monolayer,^{30,35} many important questions are pending: What is the stability of VSe_2 bulk in different phases? How do the electronic and magnetic properties vary with the bulk-phase structures? What is the stability of T - and H - VSe_2 monolayer and its 1D derivatives? How do the electronic and magnetic properties of the T - and H - VSe_2 few-layers, monolayer, nanoribbons, and nanotubes differ from the bulk? How can chemical modifications such as hydrogenation modulate the electronic properties of VSe_2 nanoribbons?

In this work, we aim to address these issues by performing density functional theory (DFT) computations.

2. MODELS AND COMPUTATIONAL METHODS

Bulk VSe_2 forms layered crystal (space group $p6_3mc$) with the separate layers stacked along the (001) direction (c -axis direction in Figure S1a). Figure 1 presents the 2D monolayer models used in this work. The T (Figure 1a) and H (Figure 1b) structural constructions are the same as TiS_2 ³⁶ and MoS_2 ,³⁷ respectively.

The structural models of the studied VSe_2 nanoribbons were constructed from the 2D monolayer slab with the cleaved plane along the (001) direction (referred to as the c -axis direction in the bulk phase, see Figure S1). As in graphene and other inorganic nanoribbons, depending on the cutting direction, two types of VSe_2 1D nanoribbons, namely, a - N with armchair edges and z - N with zigzag edges (N is the ribbon width), can be obtained. The width N is represented by the number of V atoms in a unit cell, and can be either odd or even. As an example, Figure 2 illustrates the top and side views of a -13 and z -8 ribbons in both T and H phases.

Periodic DFT computations were performed by using the plane-wave technique implemented in the Vienna *Ab initio* Simulation Package.^{38–41} The ion–electron interaction is described with the projector augmented wave^{42,43} method. The exchange–correlation energy is described by the functional of

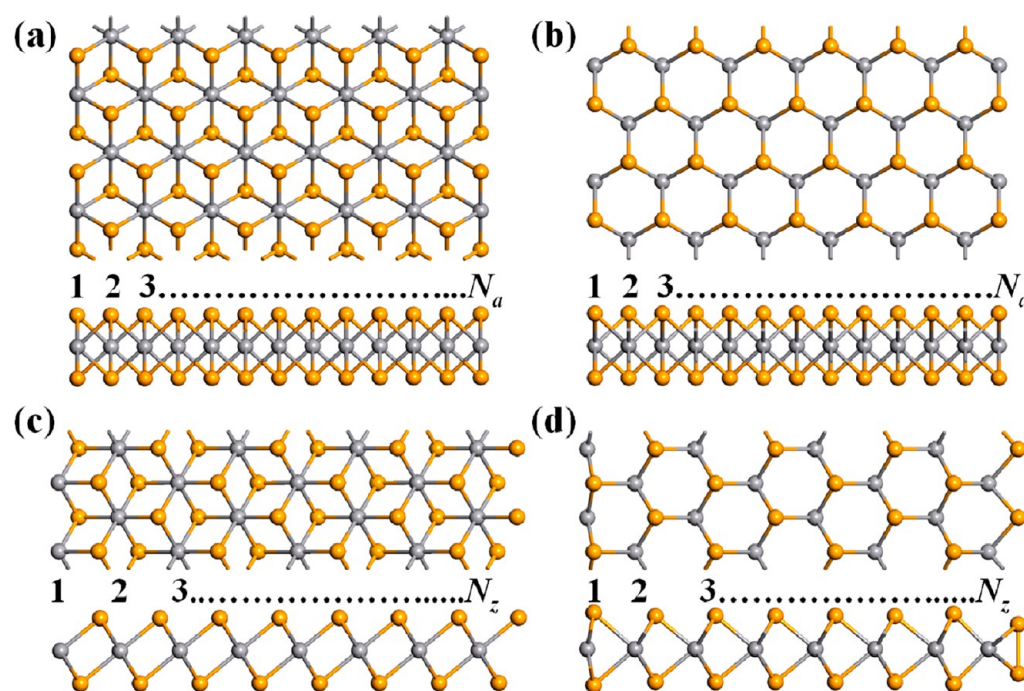


Figure 2. Geometries of the top and side views of 1D single-layered VSe₂ nanoribbons in 1T (left) and 2H (right) phases with armchair (a, b) and zigzag (c, d) edges containing two unit cells without optimization [the width $N_a = 13$ in (a) and (c), $N_z = 8$ in (b) and (d)]. The gray and khaki atoms represent V and Se atoms, respectively.

Perdew, Burke and Ernzerhof (PBE)⁴⁴ based on generalized gradient approximation with spin polarization. A 500 eV cutoff for the plane-wave basis set was used in all the computations. 1D periodic boundary condition was applied along the growth direction of the ribbons to simulate the infinitely long ribbon systems, and the supercell was large enough to ensure a vacuum spacing greater than 10 Å. For geometry optimization, the k -point grids of $8 \times 8 \times 6$, $8 \times 8 \times 1$, and $1 \times 1 \times 8$ were used for 3D bulk, 2D sheets, and 1D ribbons, respectively, while larger k -point grids ($25 \times 25 \times 1$ and 21 k points for VSe₂ nanosheet and nanoribbons, respectively; the k points for nanoribbons are with a line path in the Brillouin zone) were used for band structure computations. Note that the standard PBE functional can not well describe the van der Waals interactions between individual layers. Thus, we adopted the PBE-D2 method⁴⁵ with the inclusion of dispersion energy correction for bulk and few-layer VSe₂.

For T bulk, the optimized in-plane (a and b axis) and interlayer (c axis) lattice parameters are 3.33 and 6.17 Å, respectively, which are very close to the experimental values of 3.35 and 6.12 Å.⁴⁶ The T bulk, with an interlayer separation (d) of 3.04 Å, is a magnetic metal (Table S1, Figure S1a), in agreement with experimental observation.⁴⁷ For comparison, we also optimized the bulk VSe₂ with three H phases ($H1$, $H2$, and $H3$) with PBE-D2 method, where trigonal prismatic monolayer were stacked by tilting the crystal lattice through an angle (θ) of $\sim 17^\circ$, $\sim 16^\circ$, and $\sim 20^\circ$ from the c -axis orientation, respectively (Table S1, Figure S1b–d).

To evaluate the stabilities of VSe₂ sheets and nanoribbons, we calculated the binding energy per atom (E_b) using the following definition: $E_b = (nE_V + mE_{Se} - E_{VSe_2}) / (n + m)$, where E_V , E_{Se} , and E_{VSe_2} represent the total energies of free V atom, Se atom, and VSe₂ per unit cell, respectively, n (m) denotes the number of V (Se) atoms in a unit cell. According to this

definition, systems with larger E_b values (positive) are energetically more favorable.

For the edge-hydrogenated nanoribbons, the average binding energy per H atom is defined as $E_b = (nE_H + E_{NR} - E_{H-NR}) / n$, where E_H , E_{NR}/E_{H-NR} , and n are the energy of single H atom, total energy of pristine/hydrogenated VSe₂ NR, and number of H atoms, respectively. On the basis of this definition, systems with stronger binding strengths have larger (positive) E_b .

3. RESULTS AND DISCUSSION

3.1. 3D VSe₂ Bulk with Different Phases. Besides T bulk, we also computed three H phases, namely, $H1$, $H2$, and $H3$, for VSe₂ bulk. The T bulk has an interlayer separation (d) of 3.04 Å, while the corresponding separations between layers in $H1$, $H2$, and $H3$ phases are 3.13, 3.20, and 3.25 Å (Table 1), respectively. These four considered bulk phases have the same stability as indicated by the same binding energy per atom (5.22 eV). Meanwhile, our computations show that these four phases of VSe₂ bulk are all ferromagnetic metals (the magnetic moments are 0.54, 2.68, 1.82, and 2.72 μ_B per unit cell for T , $H1$, $H2$, and $H3$ phases, respectively; see Figure S1).

3.2. Pristine 2D Monolayer and Few-Layer VSe₂ Sheets with Different Phases. Very recently, Xie's group successfully obtained ultrathin VSe₂ nanosheets with thicknesses ranging from 2.28 to 4.65 nm (about four to eight Se–V–Se atomic layers),³⁰ and their band structure computations revealed that the T -type monolayer is magnetic metallic. Here, we studied VSe₂ monolayer of both T and H phases (Figure 1), and few-layer VSe₂ nanosheets in T , $H1$, $H2$, and $H3$ phases (Figure S1). The number of Se–V–Se atomic layers for the few-layer nanosheets was chosen as 2, 3, 4, and 8.

For VSe₂ monolayer, the Se–V bonds in T and H phases are 2.48 and 2.50 Å, respectively, and the corresponding Se...Se distances are 3.69 and 3.20 Å. The thickness of the T monolayer is 3.15 Å, slightly larger than that in bulk counterpart (3.13 Å).

Table 1. Calculated Binding Energies per Atom (E_b , in eV), Interlayer Separations (d , in Å), and Magnetic Moments (M , in μ_B) of T -, $H1$ -, $H2$ -, and $H3$ - VSe_2 Monolayer, Two-Layer, Three-Layer, Four-Layer, Eight-Layer, and Bulk

	monolayer	two-layer	three-layer	four-layer	eight-layer	bulk
<i>T</i> - VSe_2						
E_b	4.95	5.18	5.19	5.20	5.21	5.22
d		3.04	3.04	3.04	3.04	3.04
M	0.44	1.01	1.53	2.07	3.12	0.54
<i>H1</i> - VSe_2						
E_b	4.97	5.19	5.20	5.21	5.21	5.22
d		3.13	3.13	3.13	3.13	3.13
M	1.00	1.89	2.78	3.67	7.23	2.68
<i>H2</i> - VSe_2						
E_b	4.97	5.19	5.20	5.21	5.21	5.22
d		3.20	3.20	3.20	3.20	3.20
M	1.00	1.90	2.80	3.71	7.35	1.82
<i>H3</i> - VSe_2						
E_b	4.97	5.18	5.19	5.20	5.20	5.22
d		3.26	3.26	3.26	3.26	3.25
M	1.00	1.89	2.79	3.70	7.31	2.72

The binding energies per atom for T - VSe_2 monolayer (E_b , 4.95 eV) is a little weaker than that of bulk phase (5.22 eV), while the E_b of the H monolayer (4.97 eV) is slightly stronger than that of the T monolayer. This relative stability trend is

similar to the case of the VS_2 monolayer.⁴⁸ The electronic structure of the T monolayer resembles that of the bulk very closely: a ferromagnetic metal with the magnetic moment of 0.44 μ_B per unit cell (Figure 1a), in line with Ma et al.'s recent theoretical results.³⁵ In comparison, the slightly more stable H monolayer is ferromagnetic semiconducting (1.00 μ_B per unit cell) with a narrow indirect band gap (~ 0.19 eV, Figure 1b), which is consistent with Pan's DFT study.⁴⁹ The magnetism of T and H monolayers originates from the V atom, as indicated by the magnetism distributions (Figure 1a and 1b).

We then extended our studies to the stability and magnetic and electronic properties of the 2D VSe_2 few-layer nanosheets. The interlayer separations (d) of the T -type, $H1$ -type, and $H2$ -type two-, three-, four-, and eight-layer sheets are the same as that in bulk (3.04, 3.13, and 3.20 Å, respectively), while the d value of the $H3$ -phase few-layer sheets (3.26 Å) are slightly enlarged with respect to that in their corresponding bulk phase (3.25 Å). As expected, the binding energy per atom (E_b) increases as the number of Se–V–Se atomic layers increases (Table 1), but the E_b values of eight-layer nanosheets, the thickest few-layer we studied, are still slightly smaller than those of bulk. Among the four phases, the two-layer ($E_b = 5.18$ eV), three-layer ($E_b = 5.19$ eV), and four-layer ($E_b = 5.20$ eV) sheets in T and $H3$ phases have lower stabilities, and the eight-layer sheets in T , $H1$, and $H2$ phases possess the same binding energy per atom (5.21 eV), and are only slightly more favorable

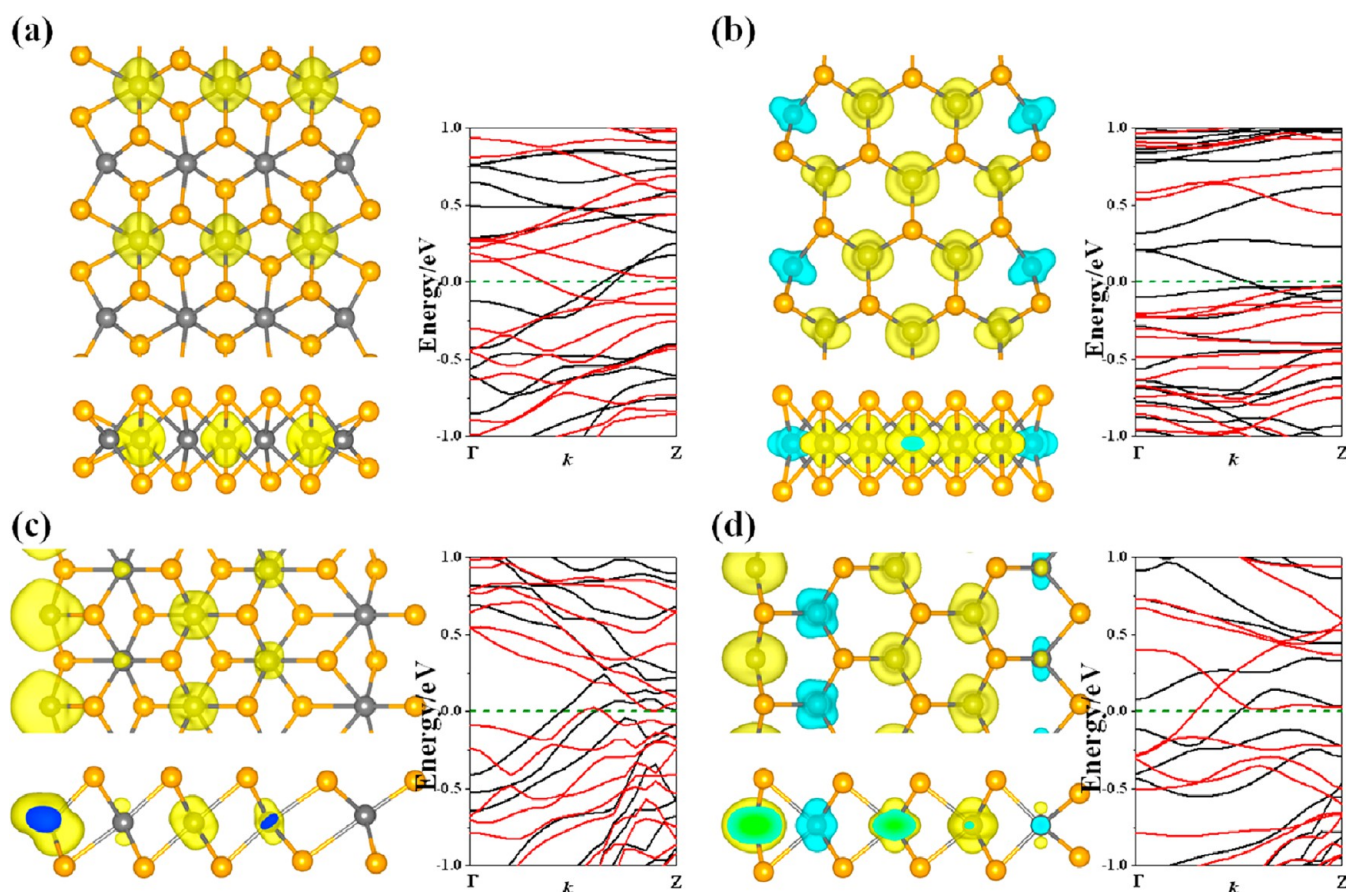


Figure 3. Magnetism distributions (top and side views) of pristine a -7 nanoribbons (1×2 supercell) in the T (a) and H phases (b), and pristine z -5 nanoribbons (1×2 supercell) in the T (c) and H phases (d), as well as their corresponding band structures. The gray and khaki atoms represent V and Se atoms, respectively. The isosurface value was set to be 0.008 $e/\text{\AA}^3$. The spin-polarized band structures with both spin-up and spin-down channels are presented in black and red, respectively. The Fermi energy is denoted by a green dashed line.

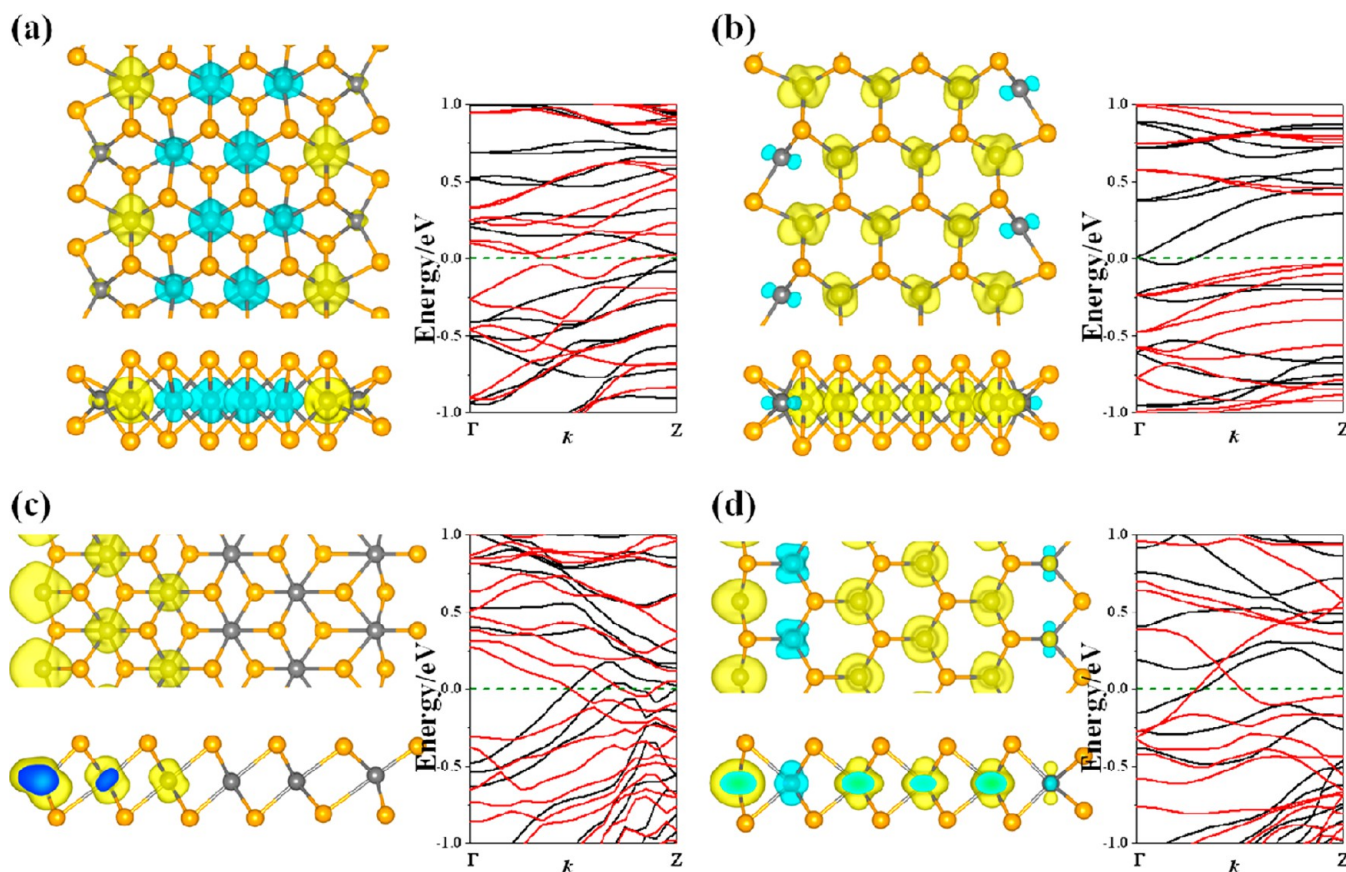


Figure 4. Magnetism distributions (top and side views) of pristine a-8 nanoribbons (1×2 supercell) in the *T* (a) and *H* phases (b), and pristine z-6 nanoribbons (1×2 supercell) in the *T* (c) and *H* phases (d), as well as their corresponding band structures. The gray and khaki atoms represent V and Se atoms, respectively. The isosurface value was set to be $0.008 \text{ e}/\text{\AA}^3$. The spin-polarized band structures with both spin-up and spin-down channels are presented in black and red, respectively. The Fermi energy is denoted by a green dashed line.

than H3 eight-layer ($E_b = 5.20 \text{ eV}$). The magnetic moments of few-layer sheets of these four phases all increase with increasing the number of Se–V–Se atomic layers (Table 1). Similar to the electronic properties of their bulk phases, the *T*, *H1*, *H3*, and *H3* few-layer sheets all maintain the metallic characteristics (Figures S2–S5).

Considering the comparable stabilities and the same metallic electronic properties of few-layer nanosheets in the four phases, it is hard to say that the experimentally obtained ultrathin VSe_2 nanosheets³⁰ with metallic character is in *T*, *H1*, *H2*, or *H3* phase, and it is very promising to synthesize the VSe_2 monolayer and nanoribbons, which may exist in both *T* and *H* phases.

3.3. 1D Bare VSe_2 Nanoribbons (NRs). Two types of nanoribbons with either armchair- or zigzag-terminated edge can be obtained depending on the cutting directions (Figure 2). Here, we considered both odd and even numbers for the width *N* and examined $N_a = 7, 8$ and $N_z = 5, 6$ as representatives.

Geometries. The optimized a-7 VSe_2 NRs of *T* and *H* phases have widths of 10.81 and 9.77 Å, respectively. The edge atoms in armchair ribbons are strongly distorted. Especially for the a-7 *T*-NR (Figure 3a), the edge Se–V armchair chains on both sides are optimized to a zigzag chain, where the edge Se atoms shift outward (inward) in the surface plane (edge plane). Consequently, the bond distances of edge Se to the edge V and subedge V are elongated to 2.25 and 2.67 Å, respectively (in comparison, the Se–V bond length in the 2D *T*- VSe_2 monolayer is 2.48 Å). For the a-7 *H*-NR (Figure 3b), the edge

Se–V armchair chains on both sides retain the armchair shape, while the edge Se atoms shift outward in the surface plane and the edge V atoms are drawn close to the edge Se, leading to the bond length of edge Se to subedge (edge) V outstretched (contracted) to 2.57 (2.30) Å, where the Se–V distance is 2.50 Å in the *H*- VSe_2 monolayer slab.

The widths of the optimized z-5 VSe_2 NRs of *T* and *H* phases are 13.35 and 12.18 Å, respectively. Both z-5 *T*- and *H*-NRs keep the zigzag edges (Figure 3c,d). On the left side, the edge Se–V bonds are shrunk to 2.32 and 2.44 Å for *T* and *H* phases, respectively, while the subedge Se–V bonds are shortened (elongated) to 2.36 (2.66) Å for z-5 *T*(*H*)-NR; on the right side, the edge and subedge Se–V bonds of z-5 *T*-NR are reduced to 2.24 and 2.44 Å, respectively, while the bond distances of edge V to inner Se (parallel to width direction) are outstretched to 2.84 Å (Figure 3c); in contrast, the edge and subedge Se–V bonds of z-5 *H*-NR are slightly elongated and shortened to 2.51 and 2.39 Å, respectively (Figure 3d).

The VSe_2 nanoribbons with even number V atoms (a-8 and z-6) for both phases have very similar edge reconstructions with the odd numbered NRs (a-7 and z-5), as shown in Figure 4. The optimized a-8 and z-6 VSe_2 nanoribbons of *T* (*H*) phase have the widths of 12.56 (12.27) and 16.34 (15.05) Å, respectively.

Stabilities. To examine the feasibility to experimentally obtain the VSe_2 NRs, we calculated the binding energy per atom (E_b) as the indicator to evaluate their thermodynamic stabilities.

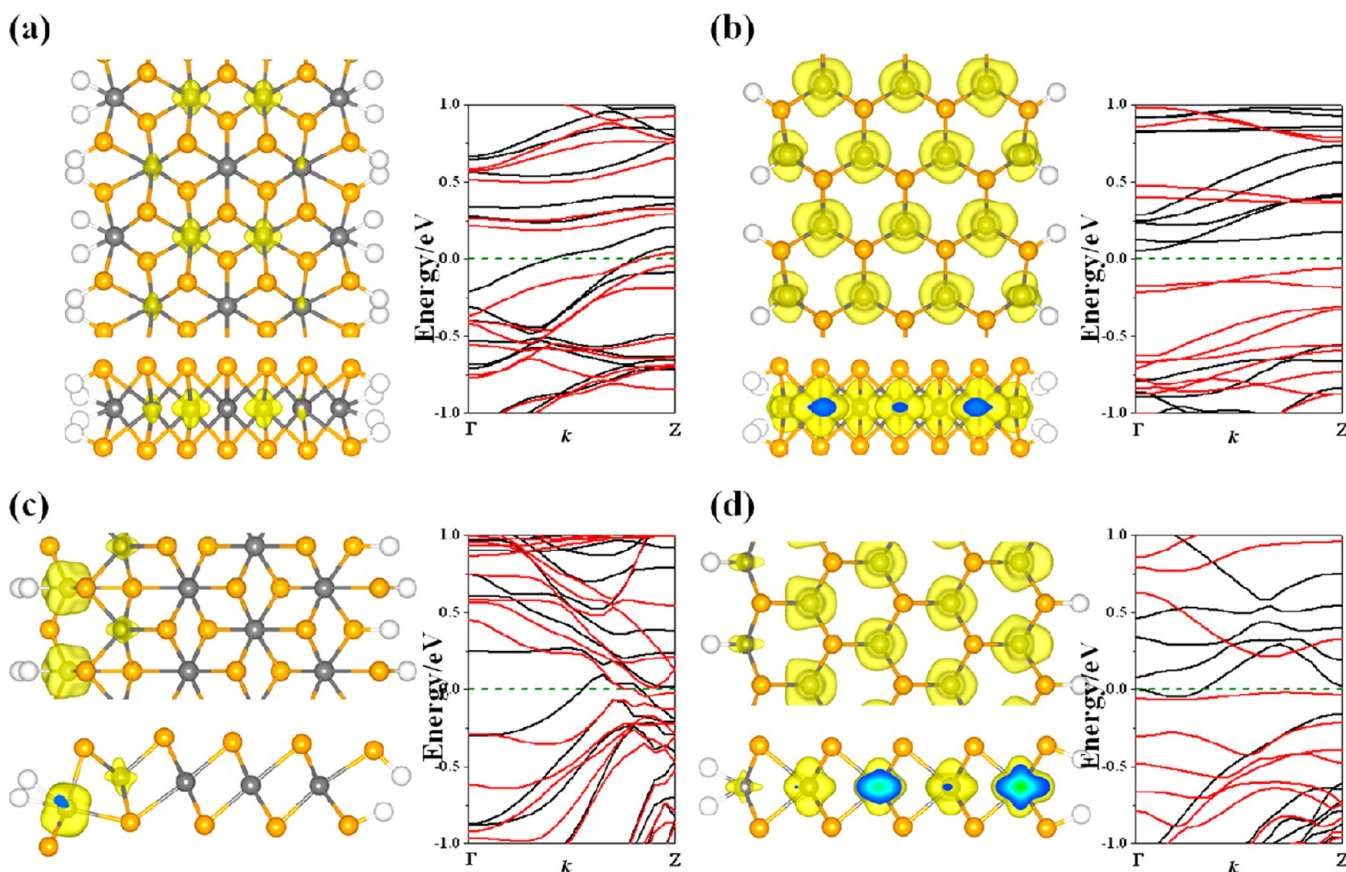


Figure 5. Magnetism distributions (top and side views) of edge-hydrogenated a-7 nanoribbons (1×2 supercell) in the *T* (a) and *H* phases (b), and edge-hydrogenated z-5 nanoribbons (1×2 supercell) in the *T* (c) and *H* phases (d), as well as their corresponding band structures. The gray and khaki atoms represent V and Se atoms, respectively. The isosurface value was set to be $0.008 \text{ e}/\text{\AA}^3$. The spin-polarized band structures with both spin-up and spin-down channels are presented in black and red, respectively. The Fermi energy is denoted by a green dashed line.

For the *T*-VSe₂ nanoribbons, the armchair NRs are more stable, the a-7 and a-8 NRs have the same binding energy per atom (4.89 eV), larger than that of the zigzag NRs (4.75 and 4.78 eV for z-5 and z-6, respectively). In contrast, for the *H*-VSe₂ nanoribbons, the zigzag NRs are thermodynamically more preferred than the armchair NRs (the E_b values for z-5, z-6, a-7, and a-8 NRs are 4.84, 4.86, 4.76, and 4.82 eV, respectively).

We further examined the stabilities of a-13 and z-8 as representatives for the NRs with larger width. As expected, the binding energy increases as the ribbon width increases. The binding energies of a-13 and z-8 *T* (H)-NRs are 4.92 (4.88) and 4.82 (4.89) eV per atom, respectively, whose widths and magnetic moments are 20.90 (20.61) and 22.17 (20.87) Å and 8.28 (4.51) and 5.61 (5.39) μB per unit cell, respectively.

For the short-width NRs we considered above, with the same width, energetically the zigzag NRs of *H* phase are slightly more favorable than those in *H* phase, while the armchair NRs prefer the *T* phase. However, the binding energy difference between the armchair and zigzag NRs in different phases will diminish with increasing the ribbon width. Thus, we expect that the experimentally synthesized nanoribbons with wider width have comparable E_b values, and may exist in both *T* and *H* phases.

Magnetic and Electronic Properties. Regardless of the ribbon width, both armchair and zigzag NRs of *T* and *H* phases are ferromagnetic. The magnetic moments of *T* (H) a-7, a-8, z-5, and z-6 nanoribbons are 2.34 (2.81), 0.05 (3.65), 2.71 (2.07), and 3.25 (3.46) μB per unit cell, respectively. The same

as the monolayer, the ferromagnetism of VSe₂ NRs arises from the 3d orbitals of the V atoms (Figures 3 and 4).

Both 1D armchair and zigzag *T* nanoribbons retain the metallic character of its 2D monolayer as indicated by the bands crossing the Fermi level in both spin-up and spin-down channels (Figure 3a,c and Figure 4a,c). However, the electronic properties of *H*-VSe₂ NRs rely on the cutting ways and differ from that of 2D monolayer: the armchair NRs are half-metallic independent of the width (Figure 3b and 4b), while the zigzag NRs display a metallic behavior regardless of the ribbon width (Figure 3d and Figure 4d) as the *T*-VSe₂ NRs with zigzag edges.

3.4. Hydrogenated VSe₂ Nanoribbons. Since the edge atoms in the bare armchair and zigzag NRs are coordinately unsaturated, it is necessary to explore how the magnetic and electronic properties of VSe₂ nanoribbons rely on edge termination. Hydrogenation is an efficient way to saturate the dangling bonds, and we investigated the edge-hydrogenated VSe₂ nanoribbons to study the underlying transformations of their electronic and magnetic properties, which is indeed an efficient computational tool and could be a guideline for controlling experimental conditions to reach the desired nanodevices. In this regard, a-7, a-8, z-5, and z-6 NRs were chosen as the representatives to investigate the edge hydrogenation effect.

When the edge dangling bonds are saturated by H atoms, both armchair and zigzag NRs in either *T* or *H* phase become less distorted, as illustrated in Figures 5 and 6. The average binding energies of H at the edge site for *T* (H) a-7, a-8, z-5,

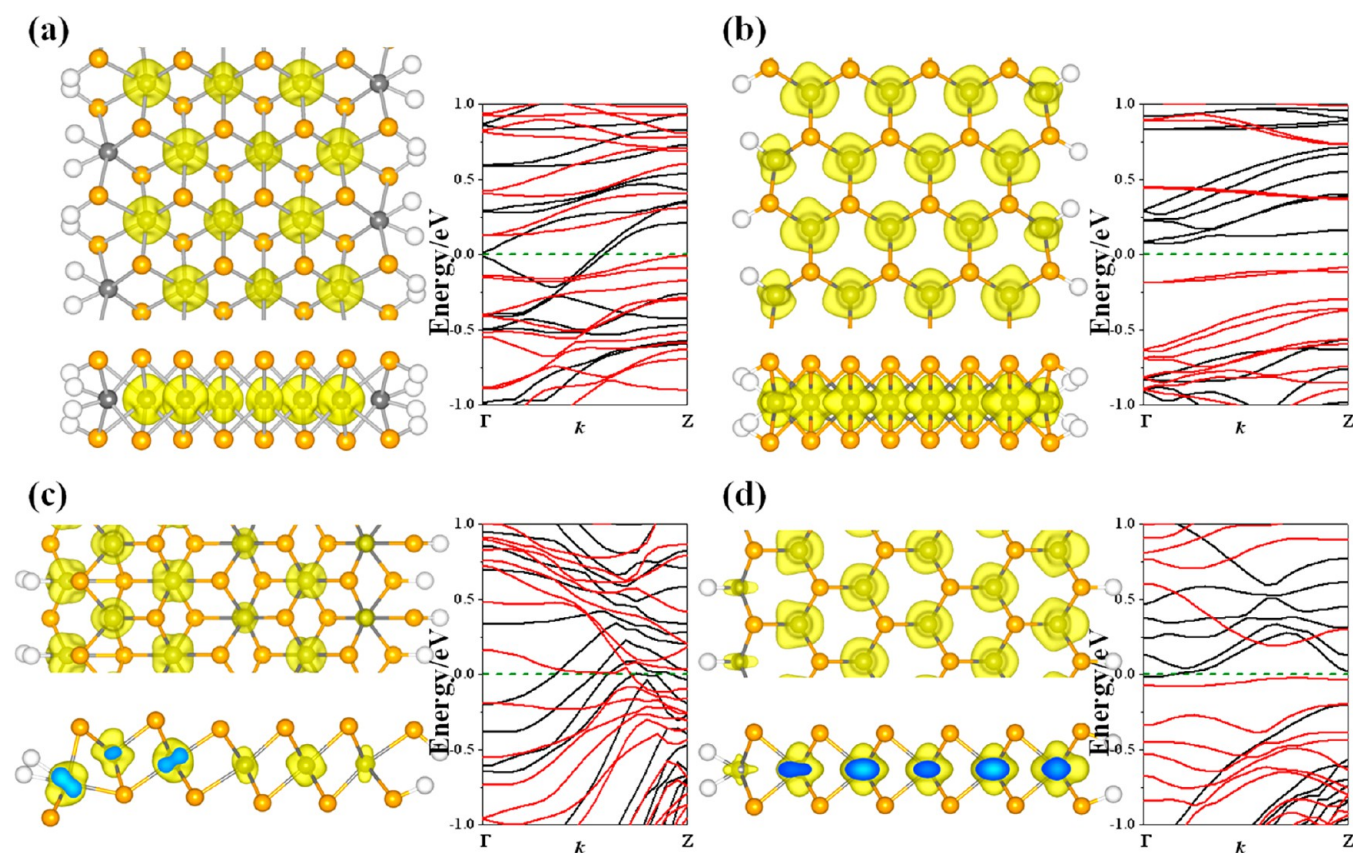


Figure 6. Magnetism distributions (top and side views) of edge-hydrogenated a-8 nanoribbons (1×2 supercell) in the *T* (a) and *H* phases (b), and edge-hydrogenated z-6 nanoribbons (1×2 supercell) in the *T* (c) and *H* phases (d), as well as their corresponding band structures. The gray and khaki atoms represent V and Se atoms, respectively. The isosurface value was set to be $0.008 \text{ e}/\text{\AA}^3$. The spin-polarized band structures with both spin-up and spin-down channels are presented in black and red, respectively. The Fermi energy is denoted by a green dashed line.

and z-6 ribbons are 1.88 (2.18), 1.90 (2.06), 2.55 (2.24), and 2.55 (2.07) eV, respectively.

The hydrogenated nanoribbons keep the ferromagnetic behavior of the bare nanoribbons. For *T*-NRs, the edge-hydrogenated a-7, z-5, and z-6 NRs retain the metallic character of the pristine NRs (Figure 5a,c and Figure 6c), while edge hydrogenation converts the metallic a-8 NR to half-metallic (Figure 6a). For *H*-NRs, hydrogen saturation transforms the original metallic z-5 and z-6 NRs to half-metals (Figure 5d and Figure 6d), while converting the pristine half-metallic a-7 and metallic a-8 NRs into semiconductors (Figure 5c and 6c). The partial charge density distributions of the edge-hydrogenated a-7 and a-8 *H*-NRs are very similar (Figure 7a–d). The valence band maximum (VBM) of the spin-up (spin-down) channel is largely composed of the edge side (edge and subedge) V atoms, and the conduction band minimum (CBM) is distributed onto the inner (edge) V atoms.

Note that the 3d transition-metal chalcogenides possess subtle electron correlation effects, particular on electronic and magnetic properties. Therefore, we also used PBE+U ($U = 3 \text{ eV}$) method to examine selected VSe_2 bulk (*T* and *H1* phases), monolayer (*T* and *H* phases), bare (z-5 *T*-NR and z-6 *H*-NR), and hydrogenated nanoribbons (a-8 *T*-NR and a-7 *H*-NR). The PBE+U lattice parameters are larger than the PBE-D2 and experimental data, for example, the optimized in-plane (*a* and *b* axis) and interlayer (*c* axis) lattice parameters of *T* bulk are 3.46 and 6.32 Å, respectively, while the corresponding PBE-D2 (experimental) values are 3.33 (3.35) and 6.17 (6.12) Å. PBE+U gives the same binding energies per atom for

T- and *H1*-bulk/monolayer, as PBE does. Compared with PBE results, PBE+U predicts the same relative stabilities and electronic properties for bare and edge-hydrogenated nanoribbons (the band structures from PBE+U calculations are shown in Figure S6), but much larger magnetic moments, for example, the magnetic moments of *T* bulk, bare z-5, and hydrogenated a-8 *T*-NRs are predicted to be 1.18, 6.68, and 8.22 μ_B , respectively, while PBE yields the corresponding values of 0.54, 2.71, and 3.84 μ_B . Since PBE gives the same trend as PBE+U for the stabilities, electronic band structures, and magnetic properties, we used the PBE data for discussions in this work.

3.5. VSe_2 Nanotubes. Since folding nanoribbons can lead to nanotubes, we also investigated the stabilities and magnetic/electronic properties of VSe_2 nanotubes, for which (10,0) and (5,5) nanotubes were chosen to represent zigzag and armchair tubes.

The binding energies of (10,0) and (5,5) VSe_2 nanotubes in *T* phase (4.76 and 4.72 eV per atom, respectively) are stronger than those in *H* phase (4.71 and 4.62 eV per atom, respectively), but lower than those of nanoribbons because of the highly strained structures in VSe_2 nanotubes.

Compared to the ferromagnetic and metallic *T* armchair/zigzag nanoribbons, the *T* (5,5) nanotube with the diameter of 13.45 Å is ferromagnetic (10.52 μ_B per unit cell) and half-metallic (Figure 8a); the *T*-(10,0) tube (Figure 8b), whose diameter is 14.93 Å, is also a ferromagnetic half-metal (20.85 μ_B per unit cell).

In contrast to the versatile electronic characteristics of *H* nanoribbons, both armchair and zigzag *H* VSe_2 nanotubes

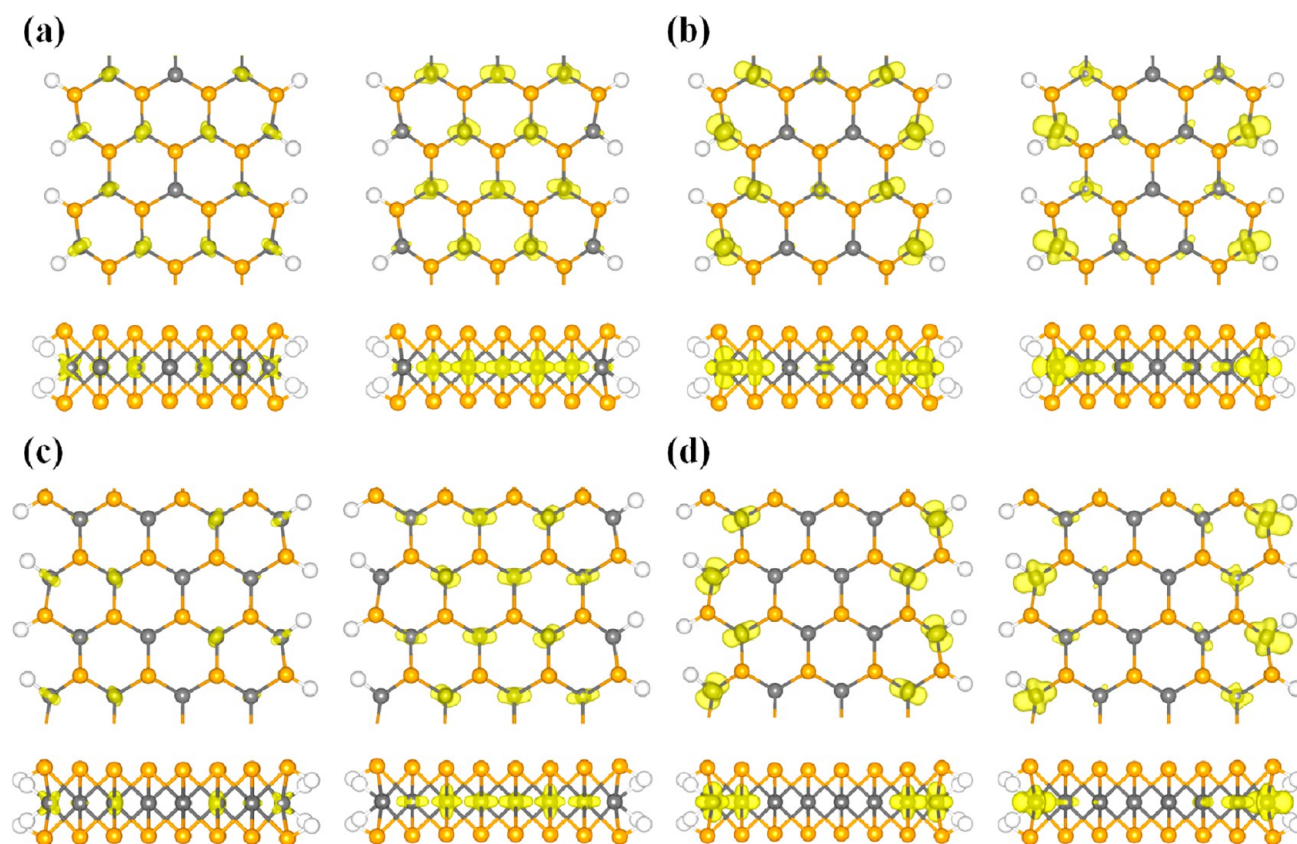


Figure 7. Partial charge densities of the top valence band (left) and bottom conduction band (right) for edge-hydrogenated H -VSe₂ a-7 nanoribbon of spin-up (a) and spin-down (b) channels, and a-8 nanoribbon of spin-up (c) and spin-down (d) channels.

are ferromagnetic metals (Figure 8c,d). The diameters and magnetic moments of H -(5,5) and H -(10,0) VSe₂ tubes are 13.22 and 14.97 Å and 5.61 and 3.15 μ_B per unit cell, respectively.

The strain energies (E_{str}) of (5,5) and (10,0) nanotubes are 6.89 (10.65) and 11.89 (15.40) eV in T (H) phase. We then deduced the moduli of VSe₂ nanotubes following the phenomenological model based on the principles of the classical theory of elasticity, $E_{\text{str}} = \pi Y L h^3 / 12 R$, where Y , L , and h are Yang's modulus, length of the nanotube, and thickness of the monolayer, respectively. The Yang's moduli of (5,5) and (10,0) nanotubes in H phase (2.37 and 2.41 TPa, respectively) are larger than those in T phase (1.64 and 1.83 TPa, respectively). The calculated Yang's moduli of VSe₂ nanotubes are larger than the reported values (~ 1 TPa) of single-walled carbon nanotubes,⁵⁰ indicating the stronger elasticity of VSe₂ nanotubes. This phenomenon can be explained by the higher energetic expense for rolling a three-atomic layer VSe₂ to a tube than that for rolling the carbon monolayer.

Considering the high strain in the narrow (5,5) and (10,0) nanotubes, we further explored the VSe₂ (10,10) and (17,0) nanotubes as representatives with larger diameters (~ 19 Å) to gain a reliable understanding of the magnetic and electronic properties. The strain energies are dramatically reduced (as listed in Table 2), and the magnetic moments are significantly increased, while the Yang's moduli are slightly decreased (except for T -(10,10) nanotube, whose Y value is larger than that of T -(5,5) nanotube). The (10,10) and (17,0) nanotubes in either T (ferromagnetic half-metals) or H (ferromagnetic metals) phase have the same magnetic and electronic behaviors with (5,5) and (10,0) NTs (see Figure S7).

Table 2. Calculated Diameters (D , in Å), Binding Energies per Atom (E_b , in eV), Magnetic Moments (M , in μ_B), Strain Energies (E_{str} , in eV), and Yang's Moduli (Y , in TPa) of the Examined VSe₂ Nanotubes

	D	E_b	M	E_{str}	Y
T -(5,5)	13.45	4.72	10.52	6.89	1.64
T -(10,10)	19.61	4.87	21.19	5.02	1.72
T -(10,0)	14.93	4.76	20.85	11.89	1.84
T -(17,0)	19.69	4.88	35.37	8.08	1.64
H -(5,5)	13.22	4.62	5.61	10.65	2.37
H -(10,10)	18.92	4.86	17.81	6.56	2.09
H -(10,0)	14.97	4.71	3.15	15.40	2.41
H -(17,0)	19.59	4.87	29.60	10.45	2.14

4. CONCLUSION

In this work, we presented detailed DFT study on the geometric structures, stabilities, and magnetic and electronic properties of VSe₂ 3D bulk, 2D monolayer, and few-layer nanosheets in both T and H phases, as well as their derived 1D nanoribbons and nanotubes. These materials are all ferromagnetic, but have rather versatile electronic properties as summarized in Figure 9.

The 3D VSe₂ bulk in either T or H (regardless of the stacking patterns) phase has the same binding energy per atom, and exhibits ferromagnetic metallic character. VSe₂ few-layers and T monolayer retain the ferromagnetic metallic properties as their bulk structures; the H monolayer is slightly more favorable than T monolayer energetically, and is a ferromagnetic semiconductor.

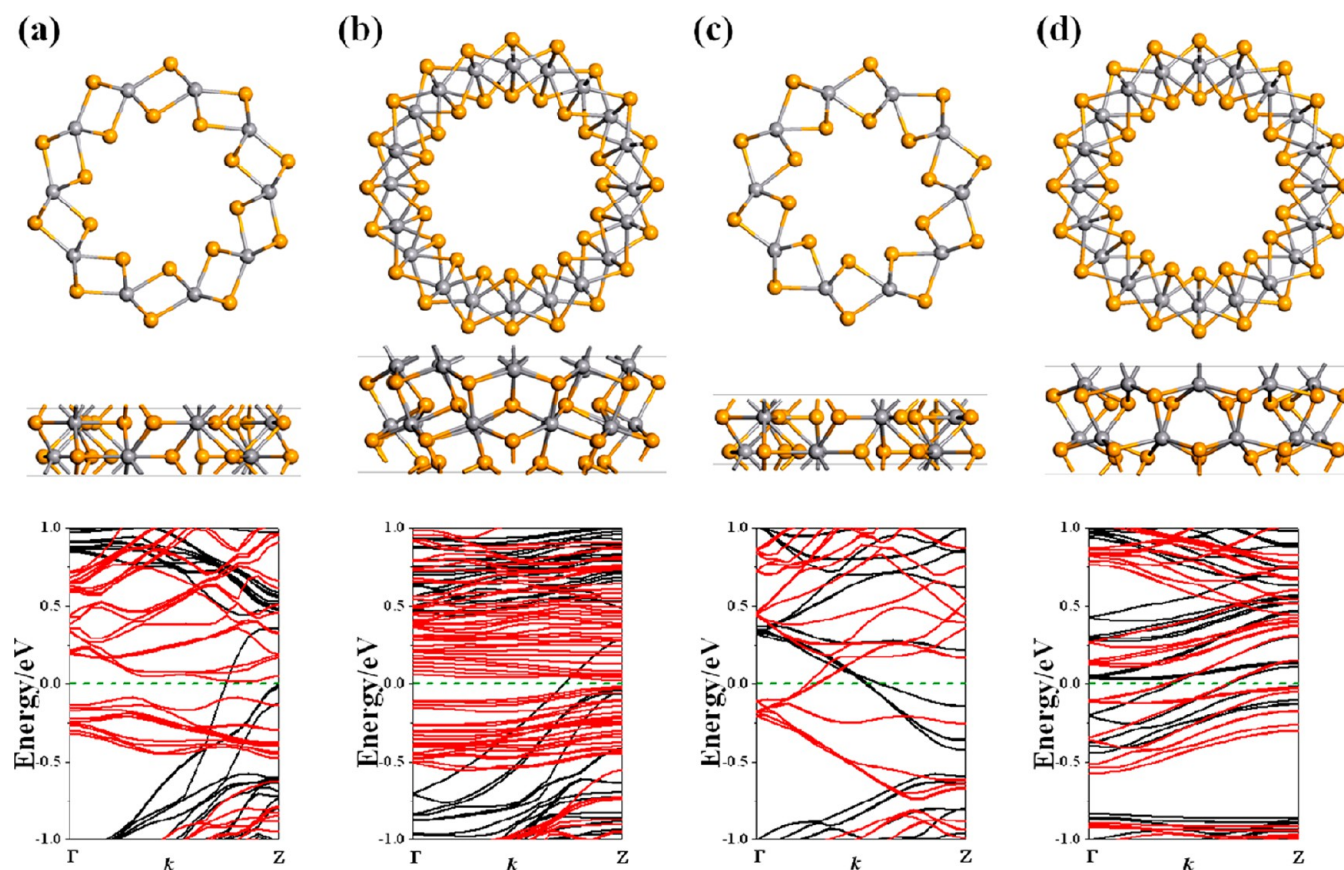


Figure 8. Top and side views of (S,S) and (10,0) nanotubes in the *T* (a, b) and *H* phases (c, d), and the corresponding band structures. The gray and khaki atoms represent V and Se atoms, respectively. The spin-polarized band structures with both spin-up and spin-down channels are presented in black and red, respectively. The Fermi energy is denoted by a green dashed line.

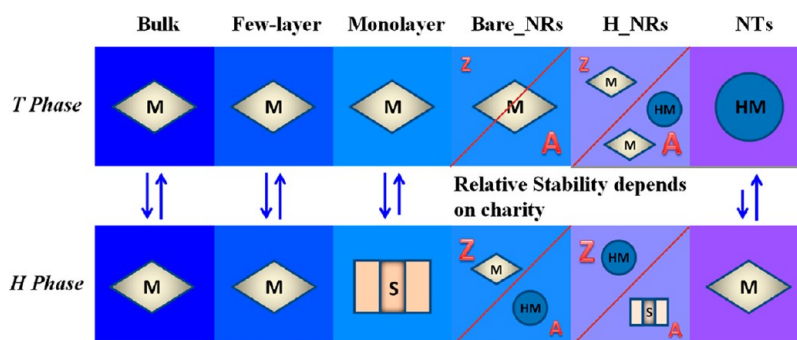


Figure 9. Relative stabilities and electronic properties of VSe₂ bulk, few-layer, monolayer, bare and hydrogenated nanoribbons, and nanotubes in *T* and *H* phases. M, HM, and S denote the metallic, half-metallic, and semiconducting properties. For NRs and hydrogenated NRs (H-NRs), and the larger Z/A, means higher stability for zigzag and armchair nanoribbons.

For the short-width bare NRs, with the same width, zigzag NRs are slightly preferred energetically in the *H* phase, while armchair NRs are more favorable in the *T* phase; the zigzag NRs in both *T* and *H* phases and the armchair NRs in *T* phase are ferromagnetic metallic, while the armchair NRs in *H* phase are ferromagnetic and half-metallic. The edge hydrogenation keeps the ferromagnetic property of the bare NRs, but retain or amend the electronic property of the pristine NRs depending on the chirality and phases.

With the same diameter, VSe₂ nanotubes in *T* phase are energetically more favorable. Regardless of the chirality,

nanotubes in *T* phase are ferromagnetic and half-metallic, while those in *H* phase are both ferromagnetic metals. The triple-atomic-layer VSe₂ nanotubes possess larger Young modulus values than those of single-walled carbon nanotubes.

The fast-growing success in isolating various 2D monolayer crystals makes us highly optimistic that monolayer VSe₂ and 1D nanoribbons can be realized experimentally in the near future. Though no *H*-VSe₂ bulk was found in experiments, the comparable/more stable monolayer and 1D nanoribbons may coexist in the *H* form with those in the *T* phase, and possess versatile electronic properties.

■ ASSOCIATED CONTENT

■ Supporting Information

The PBE-D2 lattice parameters, geometries, and band structures of T -, $H1$ -, $H2$ -, and $H3$ -VSe₂ bulk, the band structures of two-, three-, four-, and eight-layer sheets, and the geometries and the band structures of (10,10) and (17,0) VSe₂ nanotubes in both T and H phases. This material is available free of charge via the Internet at <http://pubs.acs.org>.

■ AUTHOR INFORMATION

Corresponding Author

*E-mail: zhongfangchen@gmail.com.

Notes

The authors declare no competing financial interest.

■ ACKNOWLEDGMENTS

This work was supported by the Department of Defense (Grant W911NF-12-1-0083) and NSF (Grant EPS-1010094).

■ REFERENCES

- (1) Novoselov, K. S.; Geim, A. K.; Morozov, S. V.; Jiang, D.; Zhang, Y.; Dubonos, S. V.; Grigorieva, I. V.; Firsov, A. A. Electric Field Effect in Atomically Thin Carbon Films. *Science* **2004**, *306*, 666–669.
- (2) Geim, A. K.; Grigorieva, I. V. Van der Waals Heterostructures. *Nature* **2013**, *499*, 419–425.
- (3) Tang, Q.; Zhou, Z. Graphene-Analogous Low-Dimensional Materials. *Prog. Mater. Sci.* **2013**, *58*, 1244–1315.
- (4) Wang, Q. H.; Kalantar-Zadeh, K.; Kis, A.; Coleman, J. N.; Strano, M. S. Electronics and Optoelectronics of Two-Dimensional Transition Metal Dichalcogenides. *Nat. Nanotechnol.* **2012**, *7*, 699–712.
- (5) Xu, M.; Liang, T.; Shi, M.; Chen, H. Graphene-Like Two-Dimensional Materials. *Chem. Rev.* **2013**, *113*, 3766–3798.
- (6) Chhowalla, M.; Shin, H. S.; Eda, G.; Li, L. J.; Loh, K.; Zhang, H. The Chemistry of Ultra-Thin Transition Metal Dichalcogenide Nanosheets. *Nat. Chem.* **2013**, *5*, 263–275.
- (7) Huang, X.; Zeng, Z. Y.; Zhang, H. Metal Dichalcogenide Nanosheets: Preparation, Properties and Applications. *Chem. Soc. Rev.* **2013**, *42*, 1934–1946.
- (8) Geim, A. K.; Grigorieva, I. V. Van der Waals heterostructures. *Nature* **2013**, *499*, 419–425.
- (9) Conley, H. J.; Wang, B.; Ziegler, J. I.; Haglund, R. F.; Pantelides, S. T.; Bolotin, K. I. Bandgap Engineering of Strained Monolayer and Bilayer MoS₂. *Nano Lett.* **2013**, *13*, 3626–3630.
- (10) Bayard, M.; Sienko, M. J. Anomalous Electrical and Magnetic Properties of Vanadium Diselenide. *J. Solid State Chem.* **1976**, *19*, 325–329.
- (11) Eaglesham, D. J.; Withers, R. L.; Bird, D. M. Charge-Density-Wave Transitions in 1T-VSe₂. *J. Phys. C: Solid State Phys.* **1986**, *19*, 359–367.
- (12) Giambattista, B.; Slough, C. G.; McNairy, W. W.; Coleman, R. V. Scanning Tunneling Microscopy of Atoms and Charge-Density Waves in 1T-TaS₂, 1T-TaSe₂, and 1T-VSe₂. *Phys. Rev. B* **1990**, *41*, 10082–10103.
- (13) Ekvall, I.; Brauer, H. E.; Wahlström, E.; Olin, H. Locally Modified Charge-Density Waves in Na Intercalated VSe₂ Studied by Scanning Tunneling Microscopy and Spectroscopy. *Phys. Rev. B* **1999**, *59*, 7751–7761.
- (14) Kamarchuk, G. V.; Khotkevich, A. V.; Bagatsky, V. M.; Ivanov, V. G.; Molinié, P.; Leblanc, A.; Faulques, E. Direct Determination of Debye Temperature and Electron-Phonon Interaction in 1T-VSe₂. *Phys. Rev. B* **2001**, *63*, 073107.
- (15) Gospodarev, I. A.; Eremenko, A. V.; Ignatova, T. V.; Kamarchuk, G. V.; Kolobov, I. G.; Minaev, P. A.; Syrkin, E. S.; Feodosyev, S. B.; Fil, V. D.; Soreau, L. A.; et al. Elastic Properties and Phonon Spectra of Quasi-Two-Dimensional VSe₂. *Low Temp. Phys.* **2003**, *29*, 151–154.
- (16) Terashima, K.; Sato, T.; Komatsu, H.; Takahashi, T.; Maeda, N.; Hayashi, K. Charge-Density Wave Transition of 1T-VSe₂ Studied by Angle-Resolved Photoemission Spectroscopy. *Phys. Rev. B* **2003**, *68*, 155108.
- (17) Mulazzi, M.; Chainani, A.; Katayama, N.; Eguchi, R.; Matsunami, M.; Ohashi, H.; Senba, Y.; Nohara, M.; Uchida, M.; Takagi, H.; et al. Absence of Nesting in the Charge-Density-Wave System 1T-VSe₂ as Seen by Photoelectron Spectroscopy. *Phys. Rev. B* **2010**, *82*, 075130.
- (18) Strocov, V. N.; Shi, M.; Kobayashi, M.; Monney, C.; Wang, X.; Krempasky, J.; Schmitt, T.; Patthey, L.; Berger, H.; Blaha, P. Three-Dimensional Electron Realm in VSe₂ by Soft-X-Ray Photoelectron Spectroscopy: Origin of Charge-Density Waves. *Phys. Rev. Lett.* **2012**, *109*, 086401.
- (19) Thompson, A. H.; Scanlon, J. C.; Symon, C. R. The Electrochemical Reaction of Li with VSe₂ and Implications on the Ionicity of Intercalation Compounds. *Solid State Ionics* **1980**, *1*, 47–57.
- (20) Starnberg, H. I.; Brauer, H. E.; Holleboom, L. J.; Hughes, H. P. 3D-to-2D Transition by Cs Intercalation of VSe₂. *Phys. Rev. Lett.* **1993**, *70*, 3111–3114.
- (21) Guzman, R.; Lavela, P.; Morales, J.; Tirado, J. L. VSe_{2-y}S_y Electrodes in Lithium and Lithium-Ion Cells. *J. Appl. Electrochem.* **1997**, *27*, 1207–1211.
- (22) Brauer, H. E.; Starnberg, H. I.; Holleboom, L. J.; Hughes, H. P. In Situ Intercalation of the Layered Compounds TiS₂, ZrSe₂ and VSe₂. *Surf. Sci.* **1995**, *331–333*, 419–424.
- (23) Brauer, H. E.; Ekvall, I.; Olin, H.; Starnberg, H. I.; Wahlström, E.; Hughes, H. P.; Strocov, V. N. Na Intercalation of VSe₂ Studied by Photoemission and Scanning Tunneling Microscopy. *Phys. Rev. B* **1997**, *55*, 10022–10026.
- (24) Ekvall, I.; Brauer, H. E.; Olin, H.; Starnberg, H. I.; Wahlström, E. Scanning Tunneling Microscopy and Spectroscopy of Na Intercalation in VSe₂. *Appl. Phys. A: Mater. Sci. Process.* **1998**, *66*, S197–S201.
- (25) Johannes, M. D.; Mazin, I. I. Fermi Surface Nesting and the Origin of Charge Density Waves in Metals. *Phys. Rev. B* **2008**, *77*, 165135.
- (26) Spiecker, E.; Schmid, A. K.; Minor, A. M.; Dahmen, U.; Hollensteiner, S.; Jager, W. Self-Assembled Nanofold Network Formation on Layered Crystal Surfaces During Metal Intercalation. *Phys. Rev. Lett.* **2006**, *96*, 086401.
- (27) Boscher, N. D.; Blackman, C. S.; Carmalt, C. J.; Parkin, I. P.; Prieto, A. G. Atmospheric Pressure Chemical Vapour Deposition of Vanadium Diselenide Thin Films. *Appl. Surf. Sci.* **2007**, *253*, 6041–6046.
- (28) Andrew, L. H.; Marek, J.; William, L.; Stuart, D. R.; Gillian, R. Vanadium Selenoether and Selenolate Complexes, Potential Single-Source Precursors for CVD of VSe₂ Thin Films. *New J. Chem.* **2009**, *33*, 641–645.
- (29) Yang, J.; Gao, J.; Wang, W.; Zeng, G.; Li, W.; Feng, L.; Zhang, J.; Wu, L.; Li, B. Optoelectrical Properties and Back Contact Characteristic of VSe₂ Thin Films. *J. Inorg. Mater.* **2013**, *28*, 312–316.
- (30) Xu, K.; Chen, P.; Li, X.; Wu, C.; Guo, Y.; Zhao, J.; Wu, X.; Xie, Y. Ultrathin Nanosheets of Vanadium Diselenide: A Metallic Two-Dimensional Material with Ferromagnetic Charge-Density-Wave Behavior. *Angew. Chem., Int. Ed.* **2013**, *52*, 10477–10481.
- (31) Sollmann, K. Ph.D. Thesis, Technical University of Berlin, 1995.
- (32) Pronin, I. I.; Gomoyunova, M. V.; Faradzhev, N. S.; Valdaitsev, D. A.; Starnberg, H. I. In-situ Intercalation of VSe₂(0001) with K: Direct Observation of Near-Surface Structure Transformation by Incoherent Medium-Energy Electron Diffraction. *Surf. Sci.* **2000**, *461*, 137–145.
- (33) Brauer, H. E.; Starnberg, H. I.; Holleboom, L. J.; Strocov, V. N.; Hughes, H. P. Electronic Structure of Pure and Alkali-Metal-Intercalated VSe₂. *Phys. Rev. B* **1998**, *58*, 10031–10045.
- (34) Reshak, A. H.; Auluck, S. Theoretical Investigations of the Electronic and Optical Properties of Pure and Alkali Metal Intercalated 1T-VSe₂. *Phys. B: Condens. Matter* **2004**, *349*, 310–315.
- (35) Ma, Y.; Dai, Y.; Guo, M.; Niu, C.; Zhu, Y.; Huang, B. Evidence of the Existence of Magnetism in Pristine VX₂ monolayers (X = S, Se)

and Their Strain-Induced Tunable Magnetic Properties. *ACS Nano* **2012**, *6*, 1695–1701.

(36) Ivanovskaya, V. V.; Seifert, G. Tubular Structures of Titanium Disulfide TiS_2 . *Solid State Commun.* **2004**, *130*, 175–180.

(37) Wilson, J. A.; Yoffe, A. D. The Transition Metal Dichalcogenides Discussion and Interpretation of the Observed Optical, Electrical and Structural Properties. *Adv. Phys.* **1969**, *18*, 193–335.

(38) Kresse, G.; Hafner, J. *Ab Initio* Molecular-Dynamics Dimulation of the Liquid-Metal-Amorphous-Semiconductor Transition in Germanium. *Phys. Rev. B* **1994**, *49*, 14251–14269.

(39) Kresse, G.; Hafner, J. *Ab Initio* Molecular Dynamics for Liquid Metals. *Phys. Rev. B* **1993**, *47*, 558–561.

(40) Kresse, G.; Furthmüller, J. Efficient Iterative Schemes for *Ab Initio* Total-Energy Calculations Using A Plane-Wave Basis Set. *Phys. Rev. B* **1996**, *54*, 11169–11186.

(41) Kresse, G.; Furthmüller, J. Efficiency of *Ab-Initio* Total Energy Calculations for Metals and Semiconductors Using A Plane-Wave Basis Set. *Comput. Mater. Sci.* **1996**, *6*, 15–50.

(42) Blöchl, P. E. Projector Augmented-Wave Method. *Phys. Rev. B* **1994**, *50*, 17953–17979.

(43) Kresse, G.; Joubert, D. From Ultrasoft Pseudopotentials to the Projector Augmented-Wave Method. *Phys. Rev. B* **1999**, *59*, 1758–1775.

(44) Perdew, J. P.; Burke, K.; Ernzerhof, M. Generalized Gradient Approximation Made Simple. *Phys. Rev. Lett.* **1996**, *77*, 3865–3868.

(45) Bučko, T.; Hafner, J.; Lebègue, S.; Ángyán, J. G. Improved Description of the Structure of Molecular and Layered Crystals: *Ab Initio* DFT Calculations with Van der Waals Corrections. *J. Phys. Chem. A* **2010**, *114*, 11814–11824.

(46) Wilson, J. A.; Yoffe, A. D. The Transition Metal Dichalcogenides Discussion and Interpretation of the Observed Optical, Electrical and Structural Properties. *Adv. Phys.* **1969**, *18*, 193–335.

(47) Bayliss, S. C.; Liang, W. Y. Reflectivity and Band Structure of 1T-VSe_2 . *J. Phys. C: Solid State Phys.* **1984**, *17*, 2193–2202.

(48) Zhang, H.; Liu, L.; Lau, W. Dimension-Dependent Phase Transition and Magnetic Properties of VS_2 . *J. Mater. Chem. A* **2013**, *1*, 10821–10828.

(49) Pan, H. Electronic and Magnetic Properties of Vanadium Dichalcogenides Monolayers Tuned by Hydrogenation. *J. Phys. Chem. C* **2014**, *118*, 13248–13253.

(50) Hernandez, E.; Goze, C.; Bernier, P.; Rubio, A. Elastic Properties of C and $\text{B}_x\text{C}_y\text{N}_z$ Composite Nanotubes. *Phys. Rev. Lett.* **1998**, *80*, 4502–4505.